# Chapter 8

# Prospects for Strong Coupling Between a Single Quantum Dot and Standing Wave Whispering Gallery Modes of a Semiconductor Microdisk Cavity

## 8.1 Introduction

In the previous three chapters, we have demonstrated AlGaAs microdisk cavities that, in principle, can be used for strong coupling experiments with semiconductor quantum dots. By this, we mean that the cavities have sufficiently high $Q$ and small $V_{\text{eff}}$ values that the maximum coupling rate between a single photon and a single QD in the cavity is larger than the decay rate of the cavity mode and the QD exciton. Of course, in practice, experimentally accessing the strong coupling regime will require addressing a number of technical issues, as will be reviewed in the subsequent chapter (chapter 9). In this chapter, we will assume that these experimental challenges can be overcome, and will focus on what we should expect to see when the experiments are conducted.

Recent demonstrations of vacuum Rabi splitting in systems consisting of a semiconductor microcavity and a single quantum dot (QD) [70, 71, 72] represent an important milestone in investigations of cavity QED in solid-state materials. The experimental configuration utilized in these experiments is schematically shown in fig. 8.1(a); the microcavity-QD system is incoherently pumped with an excitation beam at an energy above the bandgap of both the QD and the surrounding cavity material (usually GaAs or some form of its alloy AlGaAs). This pump light is absorbed and generates carriers in the GaAs system that can eventually (through phonon relaxation) fill the QD; under weak enough pumping conditions, a single electron-hole pair can fill the QD, forming a bound exciton state. The electron-hole pair eventually recombines, leading to spontaneous emission that is modified by the presence of the microcavity. When the cavity is of small enough volume, the coupling ($g$) between the QD exciton and the cavity can be large, and if the cavity decay rate $\kappa$ and QD decay rate $\gamma_{\perp}$ are smaller than $g$, the system is said to be strongly coupled [9], in that the QD exciton and cavity mode are no longer truly separate entities but are instead bound together. In the experiments described in refs. [70, 71, 72], the evidence of this strong coupling has been presented in the form of spontaneous emission measurements from the QD-microcavity system, which display a double-peaked structure, rather than the single peak associated with either the cavity mode or QD exciton alone. This vacuum Rabi splitting [172, 173] is one signature of the strong coupling regime in cQED.

Applications of strongly coupled QD-microcavity systems to areas such as nonlinear optics [174, 175, 176, 177, 178] will also require an ability to effectively couple light into and out of the microcavity-QD device. That is, rather than measuring the spontaneous emission of the system alone, it is also important to have access to the cavity's response (transmission or reflection). This is true if, for example, one wants to examine the effect of a coupled QD-cavity system on the propagation of a subsequent beam through the cavity [174, 79], or if one wants to use the phase of the emerging transmitted signal within some type of logic gate [179]. Indeed, in 'traditional' cavity QED experiments, it is the cavity's transmitted or reflected signal that is typically observed [77, 17, 18, 78].

As we have described in previous chapters within this thesis, following demonstrations of coupling to *silica*-based cavities such as microspheres [32, 20] and microtoroids [56], we have shown that optical fiber tapers [122, 32] are an effective means to couple light into and out of wavelength-scale, semiconductor microcavities such as photonic crystals and microdisks. In addition, the microdisk cavities we have demonstrated are very promising for semiconductor cQED experiments, with cavity $Q$s in excess of $10^5$ for devices with $V_{\text{eff}} \sim 2\text{-}6(\lambda/n)^3$. These $Q$ values are significantly larger than those utilized in refs. [70, 71, 72], and as a result, the devices that we consider are poised to operate well within the strong coupling regime, where coherent interactions between the QD and photon occur. It is envisioned that initial experiments in this fiber-coupled microcavity-QD system (fig. 8.1(b)) will examine vacuum-Rabi splitting through measurements of the transmission spectrum past the cavity; such measurements will be directly analogous to recent measurements of vacuum Rabi splitting from one-and-the-same atom in a Fabry-Perot cavity [78].

The goal of this chapter is to provide a theoretical basis, accompanied by numerical simulations,

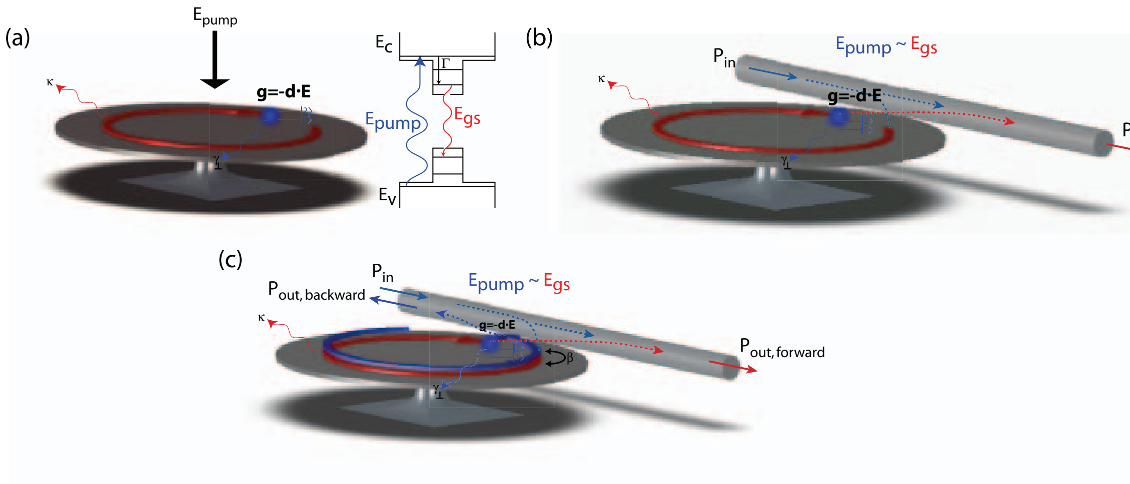


Figure 8.1: Illustrations of the various experimental configurations utilized in studying coupling between a semiconductor microcavity (microdisk in this case) and a single QD. $g$=QD-microcavity coupling rate, κ=cavity decay rate, and $\gamma_{\perp}$=QD decay rate. (a) Incoherent pumping ($E_{pump} > E_{gs}$) above the bandgap of the microcavity material. Here, strong coupling between a single QD and the microcavity mode is observed through measurements of vacuum Rabi splitting in the spontaneous emission from the QD. (b) Near-resonant driving ($E_{pump} \sim E_{gs}$) using a fiber taper to couple light into and out of the microdisk. Evidence of coupling between the QD and microcavity will be observed through measurements of the transmitted signal through the fiber taper as a function of input wavelength. (c) Near-resonant driving of a realistic microdisk-QD system, including both clockwise and counterclockwise propagating modes of the disk, and potential coupling, at a rate β, between the two modes due to surface scattering.

for the experiments to be performed with single QDs in fiber-coupled microdisk cavities. Of particular concern is the proper treatment of the whispering gallery modes (WGMs) in the cavities. More specifically, for a given polarization (TE or TM), the WGMs have a degeneracy of 2, as modes with azimuthal number $\pm m$ have the same frequency, but circulate around the disk in opposite directions. The WGMs are typically excited through an external waveguide (such as a fiber taper), and in a perfect WGM resonator, the forward propagating mode through the waveguide excites only the clockwise propagating mode in the resonator (see fig. 8.1(b)). As we have described several times within this thesis, imperfections in the resonator will change this, as they cause backscattering that can couple the clockwise (*cw*) and counterclockwise (*ccw*) propagating modes (fig. 8.1(c)). If the loss rates in the system (due to material absorption, other scattering and radiation loss, etc.) are low enough, the backscattering can lead to coherent coupling of the *cw* and *ccw* modes, producing a pair of standing wave modes. Our interest is to then study the interaction of a single quantum dot with the microdisk WGMs in the presence of this backscattering (which has been present in all of our experiments to this point), and determine the spectral response of the system for varying degrees of quantum-dot-cavity coupling ($g$), backscattering ($\beta$), and modal loss ($\kappa$). We examine how the phase of the backscattering parameter affects the coupling between one or both cavity modes and the QD, and how the QD itself serves to couple the cavity modes together.

The organization of this chapter is as follows: in section 8.2, we review the simple classical coupled mode theory for modal coupling in microdisk cavities in absence of a QD. The starting point is the analysis from section 5.2, where we have derived the coupled mode equations for backscattering-induced coupling between the clockwise and counterclockwise propagating modes in a microdisk. In section 8.2, we further develop this theory by including input-output coupling from a waveguide (appendix E). Section 8.3 presents the quantum mechanical analysis of this system in the presence of a QD. We review the quantum master equation for this system and look at semiclassical approximations for specific choices of the backscattering parameter. As we have previously noted, standing wave WGMs have half the effective modal volume of traveling wave modes, and it is therefore expected that the peak electric field strengths they sustain are $\sqrt{2}$ times larger; this is explicitly confirmed in the derivation of the quantum master equation and associated Heisenberg equations of motion. In section 8.4, we present the results of numerical solutions of the quantum master equation for parameters that are accessible in current experiments. Finally, in section 8.5, we consider low power switching as one potential experiment beyond the observation of vacuum Rabi splitting in a fiber-coupled microdisk-QD system.

## 8.2 Modal coupling of two whispering gallery modes due to surface scattering

We start by reviewing the simple (classical) coupled mode theory for surface-roughness-induced coupling of the *cw* and *ccw* whispering gallery modes in an empty microcavity [146, 135, 147, 148] (without a quantum dot). Our analysis begins where we left off in section 5.2, with the coupled mode equations:

$$\frac{da_{cw}}{dt} = -i\Delta\omega a_{cw}(t) + i|\beta|e^{i\xi}a_{ccw}(t), \tag{8.1}$$
$$\frac{da_{ccw}}{dt} = -i\Delta\omega a_{ccw}(t) + i|\beta|e^{-i\xi}a_{cw}(t), \tag{8.2}$$

These equations represent the time evolution of the two mode amplitudes $\{a_{cw},a_{ccw}\}$ of an isolated system, without loss or coupling to an external waveguide. For the experiments considered in our work, the waveguide coupler will be an optical fiber taper through which light is traveling in the forward propagating mode. Light will then be coupled into the clockwise WGM of the microdisk structure, and this can be included (appendix E) through the addition of the term *ks* to equation (8.1), where $k$ is a coupling coefficient, and $|s|^2$ is the normalized input *power* (the mode amplitudes $a_{cw,ccw}$ are normalized to *energy*). Loss is introduced to the coupled mode equations by use of the phenomenological *field* decay rate $\kappa_T$, taken to be the same for both the *cw* and *ccw* modes (though in general this does not have to be the case). This total field decay rate is broken into a contribution from intrinsic microdisk absorption and scattering loss ($\kappa_i$) and a contribution due to coupling back into the waveguide ($\kappa_e$), so that $\kappa_T = \kappa_i + \kappa_e$. Assuming lossless coupling and time reciprocity, it can be shown [125] that $|k|^2 = 2\kappa_e$. The coupled mode equations then read:

$$\frac{da_{cw}}{dt} = -\Big(\kappa_T + i\Delta\omega\Big)a_{cw}(t) + i|\beta|e^{i\xi}a_{ccw}(t) + is\sqrt{2\kappa_e} \tag{8.3}$$
$$\frac{da_{ccw}}{dt} = -\Big(\kappa_T + i\Delta\omega\Big)a_{ccw}(t) + i|\beta|e^{-i\xi}a_{cw}(t), \tag{8.4}$$

Here, the phase of the coupling coefficient was chosen to reflect the $\pi/2$ phase shift that occurs when light is coupled from the waveguide into the cavity. These two coupled equations can be rewritten as uncoupled equations in terms of the variables $a_{sw,1}$ and $a_{sw,2}$, which represent the standing wave mode amplitudes

$$\begin{aligned} a_{sw,1} &= \frac{1}{\sqrt{2}}\Big(a_{cw} + e^{i\xi}a_{ccw}\Big) \\ a_{sw,2} &= \frac{1}{\sqrt{2}}\Big(a_{cw} - e^{i\xi}a_{ccw}\Big). \end{aligned} \tag{8.5}$$

For an ideal microdisk, $a_{cw}$ and $a_{ccw}$ have an azimuthal spatial dependence of $e^{im\phi}$ (where $m$ is the azimuthal mode number and is a nonzero integer), so that $a_{sw,1}$ and $a_{sw,2}$ will have an azimuthal spatial dependence that will be a mixture of $\cos(m\phi)$ and $\sin(m\phi)$, with the precise dependence being a function of the phase $\xi$ of the backscattering parameter $\beta$.

The transmitted and reflected signals can be determined in either the basis of $\{a_{cw}, a_{ccw}\}$ or $\{a_{sw,1}, a_{sw,2}\}$; because our formulation of the problem has an external waveguide input $s$ that is a

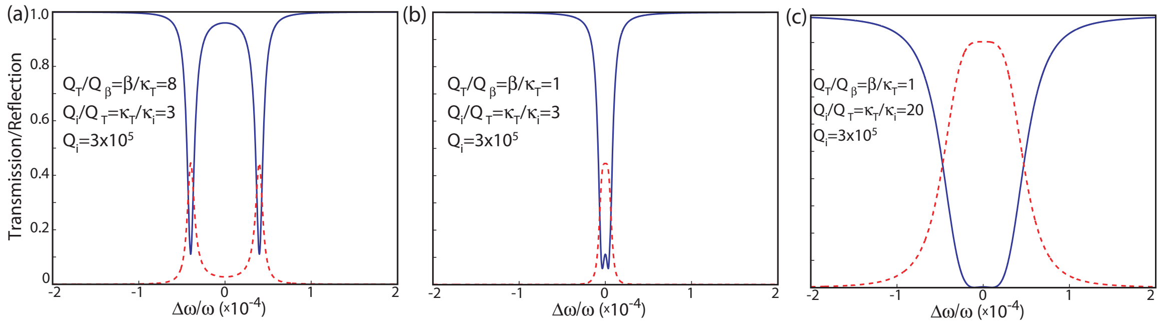


Figure 8.2: Normalized transmitted (solid line) and reflected (dashed line) signal for standing wave whispering gallery modes, determined through steady state solution of the coupled mode equations given in equation (8.3). (a) $\beta/\kappa_T = 8$, $\kappa_T/\kappa_i = 3$ (b) $\beta/\kappa_T = 1$, $\kappa_T/\kappa_i = 3$, and (c) $\beta/\kappa_T = 1$, $\kappa_T/\kappa_i = 20$. $Q_i = 3\times10^5$ in all cases.

source for $a_{cw}$, it is most natural to solve for these quantities in the traveling wave mode basis, and they are given by $|t|^2 = |-s - i\sqrt{2\kappa_e}a_{cw}|^2$ and $|r|^2 = |\sqrt{2\kappa_e}a_{ccw}|^2$ (appendix E). Steady state solutions for the normalized transmitted and reflected signals from the cavity for a number of different parameters are shown in fig. 8.2. For $\beta > \kappa_T$ (fig. 8.2(a)), we see the formation of a distinct pair of resonances, located at $\omega = \omega_0 \pm \beta$. These dips correspond to standing wave resonances that result from a backscattering rate ($\beta$) that exceeds all other losses in the system ($\kappa_T$), so that coherent coupling between the *cw* and *ccw* modes can take place. As we see in fig. 8.2(b)-(c), for $\beta \sim \kappa_T$, the resonances begin to overlap and are no longer distinguishable.

For cavity QED applications, one very important consequence of the distinction between traveling wave and standing wave modes is in the effective volume of the mode ($V_{\text{eff}}$), as the peak electric field strength (per photon) in the cavity scales as $1/\sqrt{V_{\text{eff}}}$. In particular, we recall the definition of $V_{\text{eff}}$ as:

$$V_{\text{eff}} = \frac{\int \varepsilon|\mathbf{E}(\mathbf{r})|^2}{max[\varepsilon|\mathbf{E}(\mathbf{r})|^2]}. \tag{8.6}$$

Standing wave WGMs have approximately half the volume of the traveling wave WGMs, so that the coupling rate $g$ between a single quantum dot and a single photon in a standing wave cavity mode is expected to be $\sqrt{2}$ times that when the quantum dot is coupled to a traveling wave cavity mode. This of course assumes the single QD is positioned at an antinode of the standing wave mode; alternately, if it happens to be positioned at a node, the coupling rate $g$ will be zero.

These arguments again rely upon having a physical system in which the coupling between *cw* and *ccw* modes is sufficiently strong enough compared to all other loss rates to allow for coherent modal coupling to form standing wave modes. They have also assumed that the QD does not introduce loss into the system. This is clearly not the case if the QD is strongly coupled to a cavity mode. In strong coupling, energy oscillates back and forth between the QD and the cavity, so that QD decay terms can also cause loss. In this case, we might expect that standing wave modes can be maintained provided that the modal coupling rate $\beta$ exceeds not only $\kappa_T$, but also the QD spontaneous emission rate $\gamma_{\mathrm{sp}}$ and non-radiative dephasing rate $\gamma_p$. To verify our physical intuition and understand the system in better detail, we consider a quantum master equation approach [149] to take into account the QD-field interaction.

## 8.3 Quantum master equation model

We begin by considering the Hamiltonian for an empty microdisk cavity (resonance frequency $\omega_c$) with field operators $\hat{a}_{cw}$ and $\hat{a}_{ccw}$ and mode coupling parameter $\beta$, written in a frame rotating at the driving frequency $\omega_l$ (see appendix G for details):

$$H_0 = \Delta\omega_{cl}\hat{a}^\dagger_{cw}\hat{a}_{cw} + \Delta\omega_{cl}\hat{a}^\dagger_{ccw}\hat{a}_{ccw} - \beta\hat{a}^\dagger_{cw}\hat{a}_{ccw} - \beta^*\hat{a}^\dagger_{ccw}\hat{a}_{cw} + i(E\hat{a}^\dagger_{cw} - E^*\hat{a}_{cw}), \tag{8.7}$$

where $\Delta\omega_{cl} = \omega_c - \omega_l$. Here, the clockwise (cw) propagating mode is driven by an intracavity field $E = -i\sqrt{2\kappa P_{in}}$, where $\kappa = \omega_c/2Q$ is the cavity field decay rate and $P_{in}$ is the input power into the cavity. In this and all equations that follow, Planck's constant $\hbar = 1$. From this Hamiltonian, the classical coupled-mode equations without dissipation can easily be derived through an application of Ehrenfest's theorem and assuming that quantum mechanical expectation values correspond to classical variables (i.e., $< \hat{a}_{cw} >= a_{cw}$, for example).

Modeling the QD as a two-level system, we add the term $H_1$ to the Hamiltonian (appendix G):

$$H_1 = \Delta\omega_{al}\hat{\sigma}_+\hat{\sigma}_- + ig(\hat{a}^\dagger_{cw}\hat{\sigma}_- - \hat{a}_{cw}\hat{\sigma}_+) + ig(\hat{a}^\dagger_{ccw}\hat{\sigma}_- - \hat{a}_{ccw}\hat{\sigma}_+) \tag{8.8}$$

where $\Delta\omega_{al} = \omega_a - \omega_l$ ($\omega_a$ is the frequency separation between the ground and first excited state of the QD). The equation of motion for the system's density matrix $\rho$ can then be found from the equation:

$$\frac{d\rho}{dt} = \frac{1}{i}[H_0 + H_1, \rho] + L\rho \tag{8.9}$$

where the term $L\rho = (L_1 + L_2 + L_3)\rho$ allows for the inclusion of decay through cavity loss (at a rate $\kappa$), quantum dot spontaneous emission (at a rate $\gamma_{\|}$, which we previously called $\gamma_{\mathrm{sp}}$), and phase-destroying collisional processes (at a rate $\gamma_p$), which are of particular importance for quantum dots, as unlike atoms, they are embedded in a semiconductor matrix that can serve as a phonon bath. These loss terms are given by (refs. [149, 180] and appendix G):

$$L_1\rho = \kappa(2\hat{a}_{cw}\rho\hat{a}^{\dagger}_{cw} - \hat{a}^{\dagger}_{cw}\hat{a}_{cw}\rho - \rho\hat{a}^{\dagger}_{cw}\hat{a}_{cw}) + \kappa(2\hat{a}_{ccw}\rho\hat{a}^{\dagger}_{ccw} - \hat{a}^{\dagger}_{ccw}\hat{a}_{ccw}\rho - \rho\hat{a}^{\dagger}_{ccw}\hat{a}_{ccw}) \tag{8.10}$$

$$L_2\rho = \frac{\gamma_{\|}}{2}(2\hat{\sigma}_-\rho\hat{\sigma}_+ - \hat{\sigma}_+\hat{\sigma}_-\rho - \rho\hat{\sigma}_+\hat{\sigma}_-) \tag{8.11}$$

$$L_3\rho = \frac{\gamma_p}{2}(\hat{\sigma}_z\rho\hat{\sigma}_z - \rho) \tag{8.12}$$

From this master equation, we can numerically calculate the steady state density matrix $\rho_{ss}$ and relevant operator expectation values such as $<\hat{a}^{\dagger}_{cw}\hat{a}_{cw}>_{ss}$, which will then allow us to determine the transmission and reflection spectrum of the coupled QD-cavity system, using formulas that are analogous to those used in the classical model of section 8.2. These calculations are the subject of the following section. For now, however, we consider what intuition may be gained by further analytical study of the master equation. We take operator expectation values ($<\hat{A}>= Tr(\hat{\rho}\hat{A})$ and $<\dot{\hat{A}}>= Tr(\hat{\rho}\dot{\hat{A}})$) to arrive at:

$$\begin{aligned}
\frac{d}{dt} < \hat{a}_{cw} > &= -i\Delta\omega_{cl} < \hat{a}_{cw} > + i\beta < \hat{a}_{ccw} > + g < \hat{\sigma}_- > - \kappa < \hat{a}_{cw} > + E \\
\frac{d}{dt} < \hat{a}_{ccw} > &= -i\Delta\omega_{cl} < \hat{a}_{ccw} > + i\beta^* < \hat{a}_{cw} > + g < \hat{\sigma}_- > - \kappa < \hat{a}_{ccw} > \\
\frac{d}{dt} < \hat{\sigma}_- > &= -\left(i\Delta\omega_{al} + \gamma_{\perp}\right) < \hat{\sigma}_- > + g(< \hat{\sigma}_z\hat{a}_{cw} > + < \hat{\sigma}_z\hat{a}_{ccw} >) \\
\frac{d}{dt} < \hat{\sigma}_z > &= -2g(< \hat{\sigma}_-\hat{a}^{\dagger}_{cw} > + < \hat{\sigma}_+\hat{a}_{cw} >) - 2g(< \hat{\sigma}_-\hat{a}^{\dagger}_{ccw} > + < \hat{\sigma}_+\hat{a}_{ccw} >) \\
&\quad - \gamma_{\|}(1 + < \hat{\sigma}_z >)
\end{aligned} \tag{8.13}$$

where we have noted that $[\hat{\sigma}_+, \hat{\sigma}_-] = \hat{\sigma}_z$, and have taken $\gamma_{\perp} = \gamma_{\|}/2 + \gamma_p$.

In the semi-classical approximation, we assume that expectation values of products of operators equal the product of the expectation values ($<\hat{\sigma}_z\hat{a}_{cw}> = <\hat{\sigma}_z><\hat{a}_{cw}>$, for example). Writing $\beta = |\beta|e^{i\xi}$, these equations then reduce to

$$
\begin{aligned}
\frac{d}{dt} <\hat{a}_{cw}> &= -i\Delta\omega_{cl} <\hat{a}_{cw}> + i|\beta|e^{i\xi} <\hat{a}_{ccw}> + g <\hat{\sigma}_-> - \kappa <\hat{a}_{cw}> + E \\
\frac{d}{dt} <\hat{a}_{ccw}> &= -i\Delta\omega_{cl} <\hat{a}_{ccw}> + i|\beta|e^{-i\xi} <\hat{a}_{cw}> + g <\hat{\sigma}_-> - \kappa <\hat{a}_{ccw}> \\
\frac{d}{dt} <\hat{\sigma}_-> &= -\left(i\Delta\omega_{al} + \gamma_\perp\right) <\hat{\sigma}_-> + g(<\hat{\sigma}_z><\hat{a}_{cw}> + <\hat{\sigma}_z><\hat{a}_{ccw}>) \\
\frac{d}{dt} <\hat{\sigma}_z> &= -2g <\hat{\sigma}_-> \left(<\hat{a}^\dagger_{cw}> + <\hat{a}^\dagger_{ccw}>\right) - 2g <\hat{\sigma}_+> \left(<\hat{a}_{cw}> + <\hat{a}_{ccw}>\right) \\
&\quad - \gamma_\parallel(1 + <\hat{\sigma}_z>)
\end{aligned}
\tag{8.14}
$$

From equation 8.5 of section 8.2, we expect that the first two equations above can be uncoupled if written in terms of standing wave operators:

$$
\begin{aligned}
\hat{a}_{sw,1} &= \frac{1}{\sqrt{2}}\left(\hat{a}_{cw} + e^{i\xi}\hat{a}_{ccw}\right) \\
\hat{a}_{sw,2} &= \frac{1}{\sqrt{2}}\left(\hat{a}_{cw} - e^{i\xi}\hat{a}_{ccw}\right).
\end{aligned}
\tag{8.15}
$$

Re-writing the operator evolution equations in terms of these quantities, we arrive at:

$$
\begin{aligned}
\frac{d}{dt} <\hat{a}_{sw,1}> &= -i\left(\Delta\omega_{cl} - |\beta|\right) <\hat{a}_{sw,1}> + g\frac{1+e^{i\xi}}{\sqrt{2}} <\hat{\sigma}_-> - \kappa <\hat{a}_{sw,1}> + E \\
\frac{d}{dt} <\hat{a}_{sw,2}> &= -i\left(\Delta\omega_{cl} + |\beta|\right) <\hat{a}_{sw,2}> + g\frac{1-e^{i\xi}}{\sqrt{2}} <\hat{\sigma}_-> - \kappa <\hat{a}_{sw,2}> + E \\
\frac{d}{dt} <\hat{\sigma}_-> &= -\left(i\Delta\omega_{al} + \gamma_\perp\right) <\hat{\sigma}_-> + \frac{g <\hat{\sigma}_z>}{\sqrt{2}}\left(<\hat{a}_{sw,1}> (1+e^{-i\xi}) + <\hat{a}_{sw,2}> (1-e^{-i\xi})\right) \\
\frac{d}{dt} <\hat{\sigma}_z> &= -\sqrt{2}g <\hat{\sigma}_-> \left(<\hat{a}^\dagger_{sw,1}> (1+e^{i\xi}) + <\hat{a}^\dagger_{sw,2}> (1-e^{i\xi})\right) \\
&\quad - \sqrt{2}g <\hat{\sigma}_+> \left(<\hat{a}_{sw,1}> (1+e^{-i\xi}) + <\hat{a}_{sw,2}> (1-e^{-i\xi})\right) - \gamma_\parallel(1 + <\hat{\sigma}_z>)
\end{aligned}
\tag{8.16}
$$

These equation indicate that, in this basis, we have a modified QD-photon coupling strength for each standing wave mode, which have shifted in frequency in comparison to the traveling wave modes and are now centered at $\omega_c \mp |\beta|$. For the first mode, corresponding to field operator $\hat{a}_{sw,1}$, the effective coupling strength is $g_{sw,1} = g(1+e^{i\xi})/\sqrt{2}$, while for the second mode, corresponding to field operator $\hat{a}_{sw,2}$, the effective coupling strength is $g_{sw,2} = g(1-e^{i\xi})/\sqrt{2}$. These coupling strengths are thus dependent on the phase $\xi$ of the backscattering parameter $\beta$; they can be as large as $\sqrt{2}g$ and as small as zero. This result is consistent with what we would expect based upon the physical intuition that the superposition of traveling wave modes will result in a pair of standing wave modes whose volume $V_{\text{eff}}$ is one-half that of the traveling wave modes. The two modes are phase shifted from each other in the azimuthal direction by $\pi/2$, and as a result, if the QD is positioned in the antinode of one mode ($\xi$=0, so that $g_{sw,1} = \sqrt{2}g$), it is within a node of the other mode (so that $g_{sw,2} = 0$), and vice versa for the situation when $\xi$=$\pi$. Note that these results can also easily be seen by substituting the equations for the standing wave field operators into the original Hamiltonian $H_0 + H_1$ (the two approaches are equivalent).

The semiclassical rate equations can be solved in steady state to yield information about the cavity response as a function of drive strength and detunings. In the case of a single cavity mode coupled to a two-level system, this leads to the standard optical bistability state equation (OBSE) (refs. [181, 182] and appendix G). Such a semiclassical solution might be of increased importance in the current work because of the potentially large system size that needs to be considered in the numerical simulations of the quantum master equation, due to the presence of two cavity modes. This will be particularly true when considering relatively large driving fields, which could be of interest in nonlinear spectroscopy of the system, for example, as in ref. [183]. For now, we consider a couple of simple examples, beginning with the case of $\xi$=0. Defining the following parameters:

$$
\begin{aligned}
n_s &= \frac{\gamma_\perp \gamma_\parallel}{4g^2}, \\
C &= \frac{g^2}{2\kappa\gamma_\perp}, \\
Y &= \frac{E}{\kappa} {n_s}^{-1/2}, \\
X_{sw,1} &= < \hat{a_{sw,1}} > {n_s}^{-1/2}, \\
X_{sw,2} &= < \hat{a_{sw,2}} > {n_s}^{-1/2},
\end{aligned}
\tag{8.17}
$$

we solve (in steady state) the semiclassical equations of motion in the standing wave basis (equation 8.16) to arrive at the following expression:

$$X_{sw,1} = \frac{Y}{1+\frac{4\sqrt{2}C}{2X_{sw,1}^2+(\frac{\Delta\omega_{al}}{\gamma_\perp})^2+1}+i\left(\frac{\sqrt{2}(\Delta\omega_{cl}-\beta)}{\kappa}-\frac{4\sqrt{2}C\left(\frac{\Delta\omega_{al}}{\gamma_\perp}\right)}{2X_{sw,1}^2+(\frac{\Delta\omega_{al}}{\gamma_\perp})^2+1}\right)}$$
$$X_{sw,2} = \frac{Y}{1+i\left(\frac{\Delta\omega_{cl}+\beta}{\kappa}\right)} \tag{8.18}$$

We are most interested in obtaining an expression for the transmission (or reflection) past the cavity and into our collection fiber, which will be the quantity measured in experiment. In the formalism presented in section 8.2, the transmission and reflection are given in terms of the traveling wave mode operators. These operators can easily be recovered here by adding and subtracting $X_{sw,1}$ and $X_{sw,2}$, as the standing wave mode operators are related to the traveling wave mode operators through equation (8.15).

As discussed earlier, the cases of $\xi = 0$ and $\xi$=$\pi$ (which is identical except that the roles of $X_{sw,1}$ and $X_{sw,2}$ are swapped) essentially involve coupling between a single standing wave WGM and the QD. For most choices of $\xi$, however, both WGMs will couple to the QD, but obtaining an equation analogous to the OBSE for an arbitrary $\xi$ is somewhat algebraically tedious. As a simple example, we consider $\xi = \pi/2$. In this case, it is perhaps easiest to start with the semiclassical equations of motion in the traveling wave basis (equation 8.14), from which we derive:

$$Y = \sqrt{2}X_+\frac{|\beta|}{\kappa}+\frac{\sqrt{2}X_+}{\left(1+\frac{|\beta|/\kappa}{1+i\frac{\Delta\omega_{cl}}{\kappa}}\right)}\left[\left(1-\frac{|\beta|}{\kappa}+\frac{4C}{2X_+^2+(\frac{\Delta\omega_{al}}{\gamma_\perp})^2+1}\right)+i\left(\frac{\Delta\omega_{cl}}{\kappa}-\frac{4C\left(\frac{\Delta\omega_{al}}{\gamma_\perp}\right)}{2X_+^2+(\frac{\Delta\omega_{al}}{\gamma_\perp})^2+1}\right)\right]$$
$$X_- = \frac{\frac{|\beta|}{\kappa}X_+ + Y/\sqrt{2}}{1+i\frac{\Delta\omega_{cl}}{\kappa}} \tag{8.19}$$

where $X_+ = \left(< \hat{a}_{cw} > + < \hat{a}_{ccw} >\right)n_s{}^{-1/2}$ and $X_- = \left(< \hat{a}_{cw} > - < \hat{a}_{ccw} >\right)n_s{}^{-1/2}$. From $X_+$ and $X_-$, $< \hat{a}_{cw} >$ and $< \hat{a}_{ccw} >$ can easily be found, and the transmitted and reflected signals from the cavity can be calculated.

## 8.4 Solutions to the steady state quantum master equation in the weak driving regime

The quantum master equation (QME) presented in the previous section is solved numerically using the Quantum Optics Toolbox [81, 82] for Matlab. In addition to the general framework provided by the Toolbox, the accompanying manual [81] provides many basic programs that are the basis of the calculations presented below; the PhD theses of Ben Lev [184] and Kevin Birnbaum [185] were also very helpful in this regard. We begin by considering steady state solutions, and calculate the transmitted and reflected signals from the cavity in the weak driving regime. As a starting point, we eliminate the quantum dot from the problem by taking the coupling rate $g = 0$. As expected, the resulting solutions (not displayed here) are identical to those obtained using the classical coupled mode equations and presented in fig. 8.2. Having confirmed that the QME solution is consistent with the classical solution in the empty cavity limit, we move on to study interactions with the quantum dot. To connect these simulations to ongoing experiments, we choose physical parameters consistent with the devices that we have described in this thesis.

In fig. 8.3(a), we plot the calculated $V_{\text{eff}}$ as a function of $D_{avg}$ for traveling wave modes of a microdisk, as calculated by finite-element method simulations (see chapters 5 and 7 for a review of these simulations). From these values for $V_{\text{eff}}$ we can calculate the maximum QD-photon coupling strength $g = \mathbf{d} \cdot \mathbf{E}/\hbar$, given by (see refs. [9, 110] and appendix H):

$$g = \frac{1}{2\tau_{\text{sp}}}\sqrt{\frac{3c\lambda_0^2\tau_{\text{sp}}}{2\pi n^3 V_{\text{eff}}}}, \tag{8.20}$$

where $\tau_{\text{sp}}$ is the spontaneous emission lifetime of the QD exciton, which we take as 1 ns in our calculations, consistent with what has been seen experimentally [142]. The results are plotted in fig. 8.3(b), and we see that $g/2\pi$ can be as high as $\sim$16 GHz. We note that in these calculations of $g$, the *traveling wave* mode volume was used, because it is the value that is entered directly into the quantum master equations presented in section 8.3. However, as we shall see below, in the presence of strong backscattering, standing wave modes are formed, and when coupled to a single QD, the resulting vacuum Rabi splitting is consistent with an effective coupling strength of $g\sqrt{2}$, as expected due to the decreased volume of the standing wave modes.

As discussed in chapter 7, for such modes, $Q_{rad} > 10^5$ for all but the smallest diameter disks

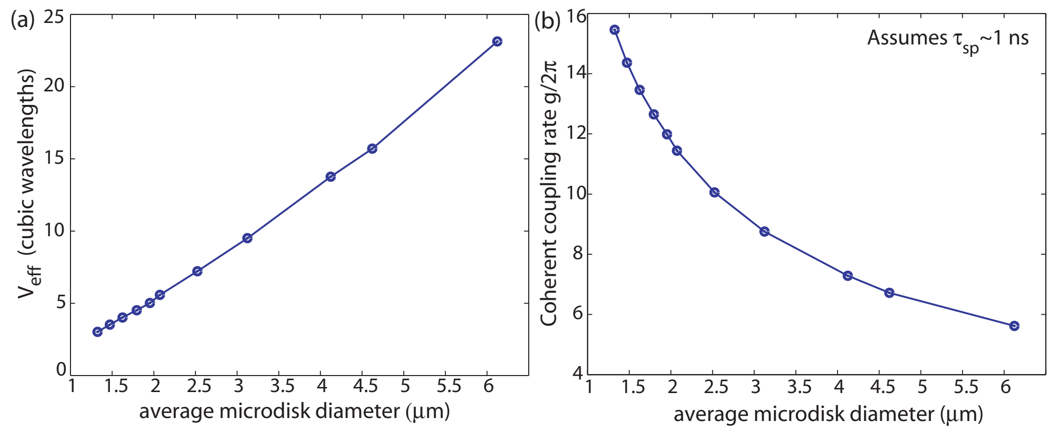


Figure 8.3: Finite-element method simulation results: (a) Modal volume $V_{\mathrm{eff}}$ as a function of microdisk diameter (taken at the center of the slab), calculated for traveling wave modes. The modes studied are $\mathrm{TE}_{p=1,m}$ WGMs with resonance wavelength within the 1200 nm band. (b) Coherent coupling rate $g/2\pi$ as a function of microdisk diameter. A QD spontaneous emission lifetime $\tau_{\mathrm{sp}} = 1$ ns is assumed in the calculation of $g$.

($D_{avg} < 1.5$ $\mu$m). We have confirmed this in experiments, with $Q$s as high as $3.6\times10^5$ achieved, so that cavity decay rates $\kappa/2\pi$ on the order of 1 GHz can reasonably be expected. Such devices exhibited doublet splittings that were on the order of 10-100 pm, corresponding to a backscattering rate $|\beta|/2\pi = $ 1-10 GHz. This rate can thus be very close in magnitude to do the QD-photon coupling rate, and we thus expect the simulation results to be particularly helpful in interpreting future experimental data.

### 8.4.1 $\beta > g > (\kappa, \gamma_\perp)$

The first situation we study is one in which the backscattering rate $\beta$ exceeds the coupling rate $g$, which in turn exceeds the cavity and QD decay rates $\kappa$ and $\gamma_\perp$. We choose $\beta/2\pi$=9.6 GHz, with $g/2\pi$=6 GHz, $\kappa/2\pi$=1.2 GHz (corresponding to $Q$=100,000), and $\tau_{\mathrm{sp}}$=1 ns ($\gamma_{\|}/2\pi \sim 0.16$ GHz). The unperturbed cavity frequency (i.e., the resonance frequency of the *traveling wave* modes) is fixed at $\omega_c = 0$, and three different QD-cavity detunings, $\Delta = \omega_a - \omega_c$=$\{0, \beta, -\beta\}$ are considered. For each value of $\Delta$, we calculate the steady state transmission and reflection spectra from the cavity in three different limits: (i) $g$=0; here, there is no QD-cavity coupling, and the response should be that of an empty cavity, (ii) $g/2\pi$=6 GHz, $\gamma_p/2\pi$=0 GHz; here, we neglect all non-radiative dephasing, which becomes a better and better approximation as the temperature of the QD-microcavity sample is lowered, and (iii) $g/2\pi$=6 GHz, $\gamma_p/2\pi$=2.4 GHz; here, we allow for a significant amount of non-

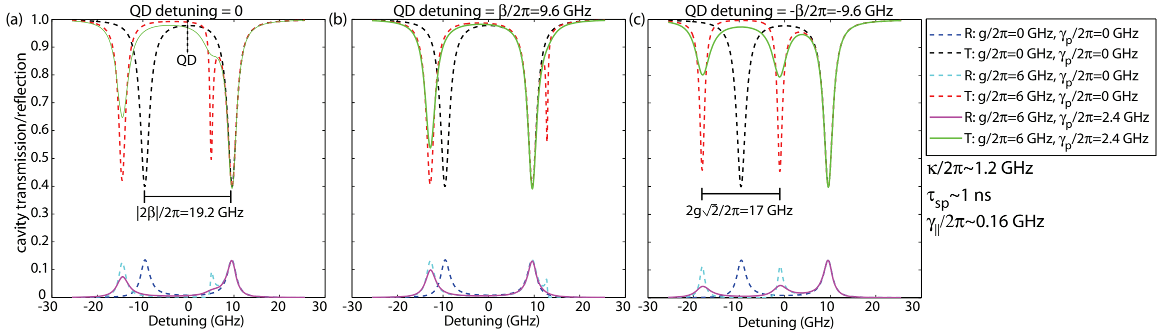


Figure 8.4: Normalized transmitted and reflected signal for a QD coupled to a microdisk cavity, calculated through numerical solution of the steady state quantum master equation under weak driving ($<$ 0.03 photons/sec input power). (a) $\Delta = \omega_a - \omega_c$=0, (b) $\Delta$=$\beta$, and (c) $\Delta$=$-\beta$. $\omega_c$ is the resonance frequency of the traveling wave whispering gallery modes. In these plots, $g/2\pi$=6 GHz, $\beta/2\pi$=9.6 GHz, $\kappa/2\pi$=1.2 GHz, and $\tau_{sp}$=1 ns.

radiative dephasing, corresponding to a QD exciton linewidth of $\sim$10 $\mu$eV (at an energy of 1 eV), which is consistent with what has been observed experimentally at temperatures of around 10-20K [142].

The results are plotted in fig. 8.4. In all of the results, we see that the primary function of $\gamma_p$ is to damp and broaden the resonances, in some cases significantly, but as expected, $\gamma_p$ does not cause the features to shift in position. In fig. 8.4(a), we see that the presence of the QD has caused the lower frequency mode to shift slightly, while the higher frequency mode has not changed position. In fig. 8.4(b), the higher frequency mode remains unshifted, and the lower frequency dip has shifted even less. Finally, in fig. 8.4(c), the higher frequency mode again remains unshifted, while the lower frequency mode has split into two resonances.

The interpretation of these results is as follows: as a result of the modal coupling due to backscattering, which has formed standing wave modes through a superposition of the initial traveling wave modes, only the lower frequency mode of the doublet has any spatial overlap with the QD, and thus, we should only expect the low frequency mode to exhibit any frequency shifts or splittings. In fig. 8.4(a), the QD, spectrally located at $\Delta$=0, is detuned from both modes (which are located at $\pm\beta$), and thus, although the low frequency mode exhibits a frequency shift, we do not see the symmetric vacuum Rabi splitting that would occur on resonance. As expected, due to the spatial misalignment, the higher frequency mode remains unshifted. In fig. 8.4(b), the QD is now on resonance with the higher frequency mode, so that it is detuned from the low frequency mode by $2\beta$. Thus, the shift exhibited by the low frequency mode is smaller than that in fig. 8.4(a). Finally in

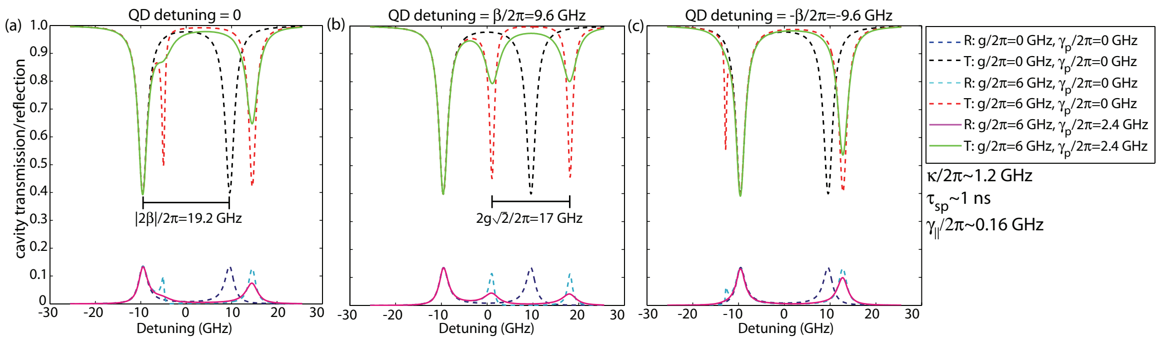


Figure 8.5: Normalized transmitted and reflected signal for a QD coupled to a microdisk cavity, calculated through numerical solution of the steady state quantum master equation under weak driving ($<0.03$ photons/sec input power). These plots are calculated using identical parameters as those used in fig. 8.4, with the exception that the phase of the backscattering parameter β has been changed from ξ=0 to ξ=π, so that β/2π=-9.6 GHz.

fig. 8.4(c), the QD is on resonance with the low frequency mode, and is also spatially aligned with it, so that we see the familiar vacuum Rabi splitting of this resonance. We note that the separation $\Omega_R$ in this case is $2g\sqrt{2}$ rather than $2g$; this is consistent with the mode volume of the standing wave modes being one half that of the traveling wave modes, as $g \sim 1/\sqrt{V_{\text{eff}}}$.

The question then arises as to what parameter preferentially selected the low frequency mode to be spatially aligned with the QD over the high frequency mode. That parameter is the phase of the backscattering rate β, which we called ξ in the previous section. For the example above, $\xi = 0$. We now consider what happens if we take $\xi = \pi$, so that β is negative. Our expectation is that this phase shift should switch which mode is spatially aligned with the QD, so that the higher frequency mode should now be selected. This prediction is confirmed in fig. 8.5, as we see that the results are the mirror image of those in fig. 8.4, where now the high frequency mode is spatially aligned with the QD and exhibits frequency shifts and vacuum Rabi splitting.

Finally, we consider an intermediate backscattering phase $\xi = \pi/2$. Here, we expect both modes to have an equal (but non-optimal) spatial alignment with the QD. For example, for modes with a $\cos(m\phi)$ and $\sin(m\phi)$ azimuthal dependence, this would correspond to having the QD located at a position where $\cos(m\phi)$=$\sin(m\phi)$ $<$, e.g., $m\phi$=$\pi/4$. The results, displayed in fig. 8.6, show that this is indeed the case. In fig. 8.6(a), for example, we see a symmetric spectrum, consistent with both modes being equally spatially coupled to the QD and equally (and oppositely) spectrally detuned from it. In fig. 8.6(b)-(c), we see that the spectra are no longer symmetric, as the QD is on resonance with the high frequency mode in fig. 8.6(b), and with the low frequency mode in fig. 8.6(c). In each

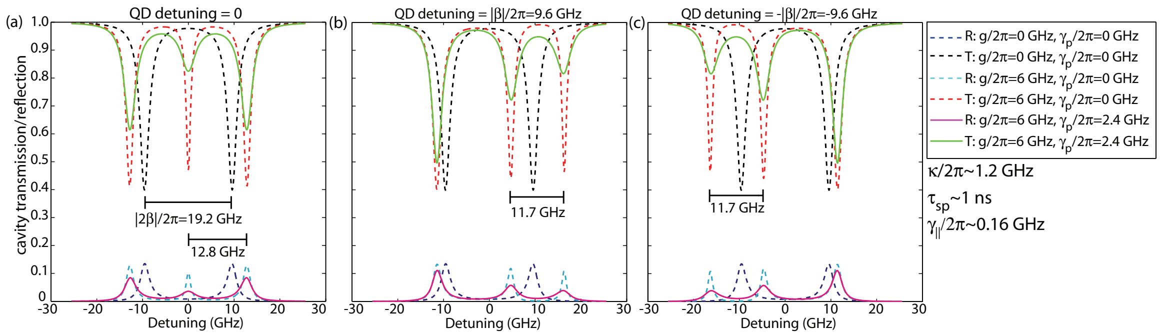


Figure 8.6: Normalized transmitted and reflected signal for a QD coupled to a microdisk cavity, calculated through numerical solution of the steady state quantum master equation under weak driving ($<$ 0.03 photons/sec input power). These plots are calculated using identical parameters as those used in fig. 8.4, with the exception that the phase of the backscattering parameter $\beta$ has been changed from $\xi$=0 to $\xi=\pi/2$, so that $\beta/2\pi=i$*9.6 GHz, where $i=\sqrt{-1}$.

case, we see Rabi splitting about the mode on resonance with the QD, and only a small shift for the non-resonant mode. The Rabi splitting between the peaks is no longer at the maximum value of $2g\sqrt{2}$, but at a value closer to $2g$. This makes sense because the maximum value of $g$ is still larger than it would be for a traveling wave mode by a factor of $\sqrt{2}$, but this gain is negated by having the QD positioned away from the peak of the field.

The situation described by fig. 8.6(a), where the QD is equally spatially coupled to the two cavity modes, and spectrally positioned in between them, might be particularly interesting, due to the presence of a transmission dip at zero laser-QD detuning. It is anticipated that this resonance can be used as a means to inject photons into the system for applications such as nonlinear switching. The advantage of this configuration, in comparison to a QD coupled to a single mode, is that the position of this zero detuning resonance is fixed, regardless of the input power. This is in contrast to what one observes for a QD coupled to a single cavity mode, where the position of the transmission dips will shift as a function of driving power, so that the amount of power that can be coupled into the cavity at a given frequency is limited.

### 8.4.2 $g>\beta>(\kappa,\gamma_{\perp})$

Here, we switch regimes slightly to one in which the QD-cavity coupling rate dominates all other rates in the system, including the backscattering rate $\beta$. In particular, we choose $g/2\pi$=12 GHz, with $\beta/2\pi$=4.8 GHz, $\kappa/2\pi$=1.2 GHz, and $\tau_{sp}$=1 ns ($\gamma_{||}/2\pi\sim0.16$ GHz). The qualitative behavior that we expect to see is identical to that of the previous section, as both $g$ and $\beta$ represent coherent processes, so that their relative values compared to each other are not as important as their values in comparison to the dissipative rates in the system. This is seen in fig. 8.7(a), where the QD is spectrally located at $-\beta$, so that it is resonant with the low frequency mode of the standing wave doublet. Predictably, the interaction with the QD causes this resonance to split, with a splitting $\Omega_R$=$2g\sqrt{2}$. The higher frequency mode remains unaffected, as the choice of $\xi$=0 causes it to be spatially misaligned from the QD.

### 8.4.3 $\kappa > g > \beta > \gamma_\perp$

Now, we take the cavity loss rate $\kappa/2\pi$=9.6 GHz to exceed both $g/2\pi$=6 GHz and $\beta/2\pi$=1.2 GHz (in addition, $\gamma_{||}/2\pi$=0.16 GHz and $\gamma_p/2\pi$=0 or 0.7 GHz), so that $\kappa > \gamma_\perp$. In the absence of a QD, we know that when $\kappa \gg \beta$, we expect to see a single transmission dip rather than a doublet. This is confirmed in simulation by the black dotted line in fig. 8.7(b). With the addition of a QD, taken to be resonant with the center frequency of the single cavity transmission dip, we expect to see this single dip split into two, with the dips not being completely resolved due to having $\kappa > g$. This is confirmed in fig. 8.7(b), where the splitting $\Omega_R/2\pi = 14.8$ GHz lies between the expected splitting for a purely traveling wave cavity mode ($\Omega_R$=$2g$) and the expected splitting for a purely standing wave cavity mode ($\Omega_R$=$2g\sqrt{2}$), and lies closer to the latter due to the degree to which $\kappa$ exceeds $\beta$.

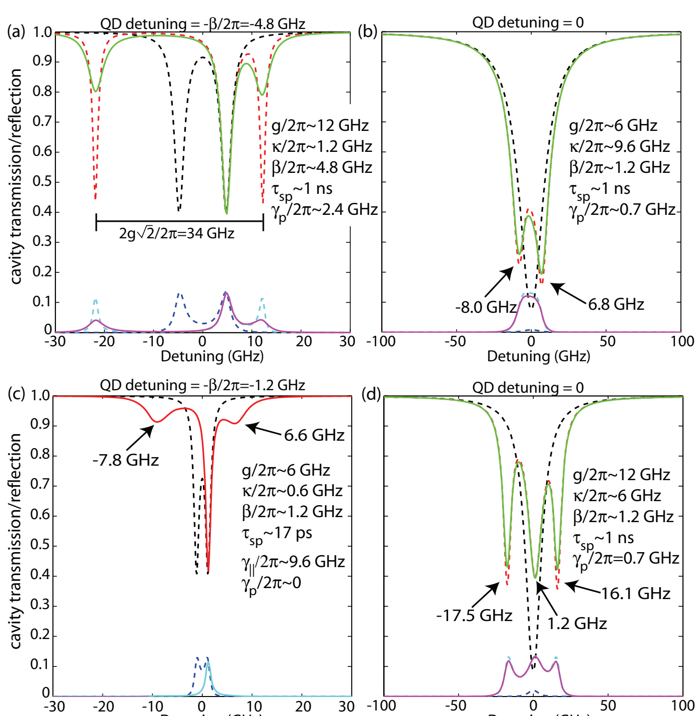


Figure 8.7: Normalized transmitted and reflected signal for a QD coupled to a microdisk cavity, calculated through numerical solution of the steady state quantum master equation under weak driving. (a) $g > \beta > (\kappa, \gamma_\perp)$, (b) $\kappa > g > \beta > \gamma_\perp$, (c) $\gamma_{||} > g > \beta > \kappa$, and (d) $g > \kappa > \beta > \gamma_\perp$.

### 8.4.4 $\gamma_{||} > g > \beta > \kappa$

Here, the roles of $\kappa$ and $\gamma_{||}$ are swapped in comparison to the previous subsection, so that $\gamma_{||}/2\pi$=9.6 GHz is the dominant dissipative rate, exceeding both $g/2\pi$=6 GHz and $\beta/2\pi$=1.2 GHz (the transverse decay rate $\gamma_{\perp} \sim 4.8$ GHz $\sim g$). Unlike our previous example, in absence of a QD, we do expect to see a pair of standing wave modes form, as $\beta > \kappa$. This is confirmed in fig. 8.7(c) (plot with the black dashed lines). Now, we introduce a QD that is spectrally aligned with the low frequency mode at $-\beta$. Because QD decay is so large in this case, however, we expect that the standing wave character of the modes is going to largely be erased when coupled to the QD; standing wave modes form only when the decay processes in the system are small enough that coherent coupling can take place between the *cw* and *ccw* propagating modes. When a QD is introduced, we expect the energy to oscillate between the QD and the cavity modes, and that standing wave modes can still form if the energy decay is not too large, both when the system is primarily 'QD-like' and 'cavity-like.' Clearly, for $\gamma_{||} \gg \beta$, this is not the case.

To confirm this intuition, we examine the calculated transmission spectrum in fig. 8.7(c). The low frequency mode does indeed split, but the splitting $\Omega_R/2\pi = 14.4$ GHz is much less than the expected splitting of $2g\sqrt{2}$ for standing wave modes, and lies much closer to the $2g$ splitting for traveling wave modes. The situation thus mimics that of the previous example. One major difference is the relatively poor contrast (transmission depth) exhibited by the split resonances; this is due to the fact that the dominant loss channel in this case, QD decay, is not collected in this measurement, unlike cavity loss (for which a large fraction is collected).

### 8.4.5 $g > \kappa > \beta > \gamma_{\perp}$

#### 8.4.5.1 Steady state analysis

Finally, we consider an intermediate scenario where QD-cavity coupling $g/2\pi = 12$ GHz is the dominant rate in the system, but where cavity decay $\kappa/2\pi$=6 GHz exceeds the backscattering rate $\beta/2\pi$=1.2 GHz. Again, in absence of a QD, we see a single transmission dip (fig. 8.7(d)), as $\kappa > \beta$. If a QD is now spectrally aligned to the center of this dip ($\Delta$=0), however, we see three dips appear within the transmission spectrum of fig. 8.7(d), as opposed to the two dips that appeared in fig. 8.7(b). The central dip is at frequency of 1.2 GHz=$\beta/2\pi$, and corresponds to the frequency of one of the two standing wave modes that can form through an appropriate combination of the traveling wave modes. As this mode is spatially misaligned from the QD, we do not expect its frequency to have shifted due to interaction with the QD. The other two dips correspond to the splitting of the low frequency standing wave mode from its original position at $-\beta/2\pi = -1.2$ GHz. The splitting of $\Omega_R/2\pi$=33.6 GHz is very close to the maximum possible value of $2g\sqrt{2}$, which is the expected value for standing wave modes (indeed, if the QD was actually spectrally aligned at $-\beta/2\pi = -1.2$ GHz, $\Omega_R$ would be even closer to $2g\sqrt{2}$).

However, the question remains as to why the picture presented is largely consistent with a QD interacting with a standing wave mode when, in absence of a QD, the system is consistent with a traveling wave mode. The basic reason is as described above; when interacting with a QD, the system oscillates between being 'QD-like' and 'cavity-like', and in each phase, undergoes decoherence due to the corresponding decay channel. As a result, the fast cavity decay rate in this example is somewhat mitigated by the very slow QD decay rate, to the point that coherent coupling between the clockwise and counterclockwise traveling wave modes can be achieved and standing wave modes can be formed.

#### 8.4.5.2 Time-dependent analysis

The density matrix calculations presented above are all steady state calculations ($\frac{d\rho}{dt} = 0$). To get a feeling for the time-dependence of the system, we can use the Quantum Optics Toolbox to numerically integrate the differential equation for the density matrix [81, 82]. One of the first things we can look at is the evolution of the cavity transmission spectrum as a function of time, to understand the time required to reach steady state. The results are plotted in fig. 8.8, along with the already calculated steady state solution. We see that the time-dependent solution approaches the steady state solution in a time of about 0.1 ns, which is on the order of the Rabi oscillation time $\tau_R \sim 1/g$.

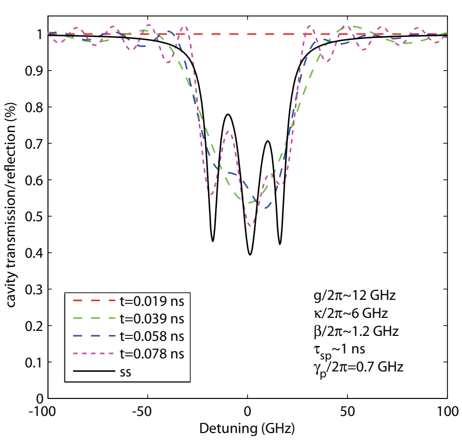


Figure 8.8: Normalized transmitted signal for a QD coupled to a microdisk cavity, calculated as a function of time through numerical integration of the quantum master equation under weak driving.

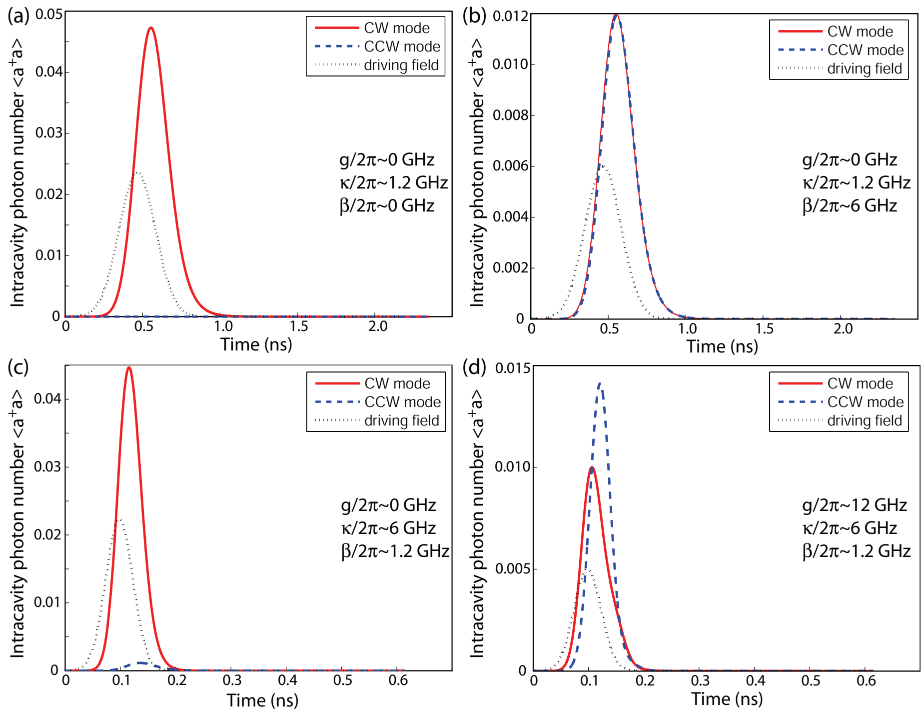


Figure 8.9: Number of intracavity photons in the microdisk clockwise (solid red curves) and counterclockwise (dashed blue curves) propagating WGMs, calculated by numerical integration of the quantum master equation. A driving field consisting of a Gaussian pulse in time is used (shown as a black dashed line), with $\omega_l$=-$\beta$. (a) $g/2\pi$=0, $\kappa/2\pi$=1.2 GHz, $\beta/2\pi$=0 GHz, (b) $g/2\pi$=0, $\kappa/2\pi$=1.2 GHz, $\beta/2\pi$=6 GHz, (c) $g/2\pi$=0, $\kappa/2\pi$=6 GHz, $\beta/2\pi$=1.2 GHz, and (d) $g/2\pi$=12 GHz, $\kappa/2\pi$=6 GHz, $\beta/2\pi$=1.2 GHz.

For the purposes of better understanding why the cavity spectrum appears as it does (and in particular, why the mode splitting is consistent with that expected for a QD interacting with a standing wave mode instead of a traveling wave mode), we examine the intracavity photon number ($<\hat{a}^{\dagger}\hat{a}>$) for the clockwise and counterclockwise modes as a function of time. Rather than using a constant (time-independent) driving field, the cavity is driven by a short pulse (Gaussian in shape, with a drive power of 0.1 photons/sec), and is centered at a frequency $\omega_l$=-$\beta$. For an ideal microdisk structure (no surface roughness) that is not coupled to a QD ($g=0$), the forward propagating mode of the fiber taper will only couple to the clockwise mode of the microdisk. This is confirmed in fig. 8.9(a), as $<\hat{a}^{\dagger}_{ccw}\hat{a}_{ccw}>$ remains zero for all times, while $<\hat{a}^{\dagger}_{cw}\hat{a}_{cw}>$ rises as light is coupled into the clockwise mode, and decays due to cavity radiation after the drive field is switched off. Next, we consider the empty cavity ($g=0$) with $\beta/2\pi$=6 GHz and $\kappa/2\pi$=1.2 GHz, so that $\beta>\kappa$. As we have described in the previous sections, in this regime, we expect to see coupling between the propagating WGMs to form standing wave modes. We thus expect to see non-zero photon numbers for both clockwise and counterclockwise modes, with the count rates damped due to cavity loss. This behavior is confirmed in fig. 8.9(b).

We now move on to the situation considered in steady state in section 8.4.5.1, starting without the QD. As the cavity decay rate $\kappa/2\pi$=6 GHz is significantly larger than the backscattering rate $\beta/2\pi$=1.2 GHz, we expect that the clockwise mode will suffer significant decay before an appreciable amount of power can be coupled into the counterclockwise mode. This is confirmed in fig. 8.9(c). Now, we introduce a QD with $\gamma_{\|}/2\pi$=0.16 GHz, and spectrally located at zero detuning (for simplicity, we have taken $\gamma_p$=0 in this calculation). The calculated steady state transmission spectrum (fig. 8.7(d)) indicated that the QD mediates coupling between the clockwise and counterclockwise modes, allowing for standing waves to form, with the low frequency mode (at $\Delta\omega = -\beta$) spatially aligned with the QD. This behavior is confirmed in fig. 8.9(d), where we see that the photon number for the counterclockwise mode increasing much more quickly than it does in fig. 8.9(c), confirming that energy transfer occurs through some process other than backscattering. Once the driving field is switched off, the photon count rates in the two modes die down, as a result of both cavity and QD decay.

The density matrix calculations performed up to this point show the evolution of the system in an ensemble-averaged sense. To provide us with further physical insight, quantum trajectory calculations can be considered [149]. In these simulations, the Schrodinger wavefunction for the system is calculated under the influence of a non-Hermitian Hamiltonian $H_{\text{eff}}$, defined in terms of collapse operators for the cavity modes and the QD. At random times within this evolution, the wavefunction is subject to collapses, corresponding to detection events. The quantum trajectory approach thus models the conditional evolution of a system, and can provide insight into what will be observed in a measurement (such as the homodyne photocurrent). If the results of many trajectories are averaged, the results of the density matrix calculations can be reproduced. This latter point has been examined in quantum trajectory simulations of the systems studied in fig. 8.9, where 50 trajectories have been averaged, and it has been confirmed that the results match those of the density matrix calculations well. As only weak driving has been thus far considered, the computational benefit of using a wavefunction-based approach rather than the density matrix is minimal. However, for future studies, both the physical insight into the dynamics of these systems and the reduction in computational cost of the quantum trajectory method may be very important.

### 8.4.6 $\beta = 0; g > \kappa > \gamma_{\perp}$

The basic result that the above examples demonstrate is that the QD can effectively serve as a means to couple the cavity modes, even in instances where the backscatter parameter is small relative to other rates in the system. As a final illustration of this, we consider the situation where the backscatter parameter is zero. In absence of the QD, we then see a single Lorentzian dip in the transmission spectrum through the fiber taper. When the QD is added, one would might expect to just see this Lorentzian dip split into two dips separated by $2g$. From fig. 8.10, we see that the mode does split, but that the splitting exceeds $2g$ (it is actually $2g\sqrt{2}$). Furthermore, we also see the presence of a Lorentzian dip at the original cavity frequency, but with the transmission contrast reduced in amplitude.

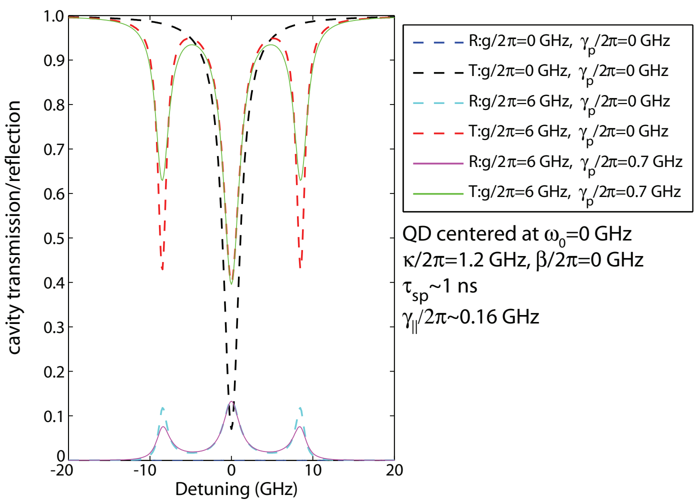


Figure 8.10: Normalized transmitted and reflected signal (steady state), for the case where the 'passive' modal coupling between clockwise and counterclockwise WGMs ($\beta$) is zero. Coupling to the atom serves to mediate coupling between the cavity modes.

The interpretation of these results is that the QD has effectively served to mediate coupling between the two traveling wave modes, creating a pair of standing wave resonances. The standing wave mode that is spatially aligned with the QD splits into the resonances at $\pm g\sqrt{2}$, while the other standing wave mode does not overlap with the QD at all, and appears as an unperturbed resonance at the original cavity frequency. Unlike the standing wave modes formed through surface-roughness-induced backscattering, this standing wave mode has not shifted in frequency with respect to the original traveling wave modes because it sees the exact same dielectric function as the traveling wave modes.[1]

[1] Standing wave modes that form through backscattering from structural variations see different dielectric functions, one which includes more of the air regions and the other that includes more of the dielectric regions, resulting in frequencies that are shifted above and below the original resonance frequency, respectively.

## 8.5 Potential for low power switching in the microdisk-QD system

The ultrasmall volumes sustained by these semiconductor microcavities offer the potential to observe phenomena in nonlinear optics at very small input powers, due to the large per photon electric field strengths within the devices. The saturation photon number, $m_0$, which represents the average number of intracavity photons needed to saturate the QD transition, can give us some idea of how low these powers might be. This quantity is given by [9]:

$$m_0 = \frac{\gamma_\perp \gamma_\parallel}{4g^2} \tag{8.21}$$

where $\gamma_\perp$ is the transverse relaxation rate given by $\gamma_\perp = \gamma_\parallel/2 + \gamma_p$ (note that $m_0$ was called $n_s$ previously). Let us first consider the case where $\gamma_p$ is small, so that the QD is radiative-limited, and $m_0 = \gamma_\parallel^2/8g^2$. For $g/2\pi \sim 10$ GHz, which is certainly reasonable for the microdisk cavities we study, and $\gamma_\parallel/2\pi \sim 0.16$ GHz ($\tau_{\mathrm{sp}} \sim 1$ ns), which is typical for self-assembled InAs QDs, $m_0 \sim 10^{-5}$. This value indicates the degree to which one photon in the cavity can affect a single QD.

To study this in a bit more detail, we use steady state solutions to the semiclassical optical bistability state equation (OBSE) and the quantum master equation (QME) to look at the cavity response as a function of the drive strength. For our purposes here, we will restrict ourselves to looking at a single (standing wave) cavity mode coupled to the QD; as we saw in the previous sections, this can occur within our system if the phase of the backscattering parameter is such that the QD is only spatially aligned with one of the two standing wave cavity modes. This simplification is also necessary as our calculations here are not done in the weak driving limit, so that a significant number of Fock space basis elements are needed to describe the cavity mode; this would become computationally untenable in the case of two cavity modes. The QME and OBSE for a single cavity mode coupled to a two-level system are discussed in appendix G.

We begin by considering a system with $(g,\kappa,\gamma_\parallel,\gamma_p)/2\pi = (6,2.4,0.16,0)$ GHz, and with the atom, cavity, and driving field all on resonance. The corresponding saturation photon number (equation (8.21)) and cooperativity parameter (equation (8.17)) are $m_0 \sim 9\times10^{-5}$ and $C \sim 94$. The critical atom number [9], which describes the number of atoms (or QDs in this case) needed to have an appreciable effect on the intracavity field, is given by $N_0 = 1/C$ and is 0.01 in this example. We first plot, on a linear scale, the normalized steady state intracavity field $X_{\mathrm{ss}} = <\hat{a}> {m_0}^{-1/2}$ as

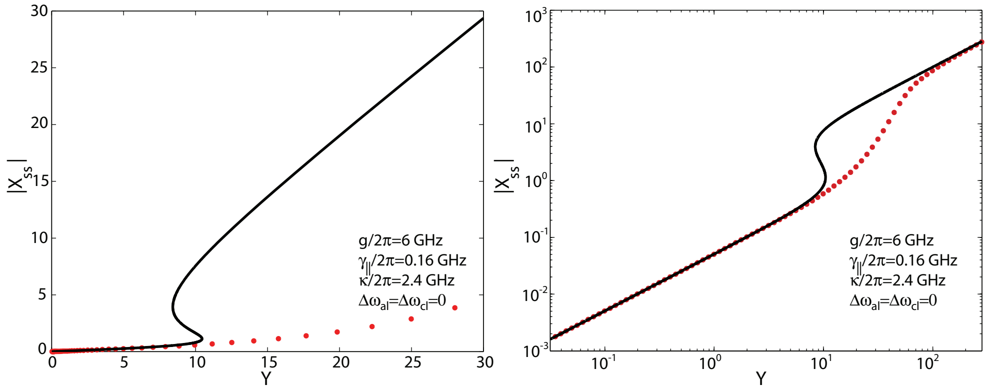


Figure 8.11: Steady state solutions to the semiclassical Maxwell-Bloch equations (solid line) and quantum master equation (dots), showing normalized intracavity field amplitude $|X_{ss}|$ as a function of normalized drive field $|Y|$. In these simulations, $\omega_a = \omega_c = \omega_l$, and $g/2\pi$=6 GHz, $\kappa/2\pi$=2.4 GHz, $\gamma_p$=0, and $\gamma_{||}/2\pi$=0.16 GHz. Correspondingly, $m_0 \sim 9 \times 10^{-5}$ and $C \sim 94$.

a function of the normalized drive field $Y = (E/\kappa){m_0}^{-1/2}$ in fig. 8.11(a). The semiclassical solution displays bistability, so that in the intermediate (multi-valued) portion of the curve, the top and bottom branches are stable solutions, and the middle branch is unstable. However, the quantum master equation solution looks very different, and the bistability has been washed away.[2] Plotted on a logarithmic scale over a wider range (fig. 8.11(b)), we confirm the absence of bistability in the quantum master equation solution, but see that it does follow the semiclassical solution in regions of small $Y$ and large $Y$.

In an experiment, we will measure the transmission or reflection response of the cavity as a function of drive power through the taper input. This is plotted in fig. 8.12, where we have displayed the cavity reflection as a function of the average number of intracavity drive photons and the input drive power, for a number of different cavity decay rates (we have assumed critical coupling between the taper and cavity). We again see that the quantum master equation solutions do not match the prediction of optical bistability that the semiclassical equation solutions make, but do indicate that switching between near-zero and unity reflection can occur for relatively small input powers, on the order of tens of nanoWatts. We note that there is a general trade-off between the contrast in reflection, which increases as the cavity $Q$ increases, and the switching power. Similar behavior can be observed in the transmitted signal by setting the laser drive frequency $\omega_l = \pm g$.

In order to achieve radiative-limited operation of the QDs, low temperatures (T$\lesssim$10 K) are required. It is interesting to consider whether functional devices can be created that operate at room

[2]This discrepancy has been observed and discussed by several authors in the context of atomic cQED [176, 186].

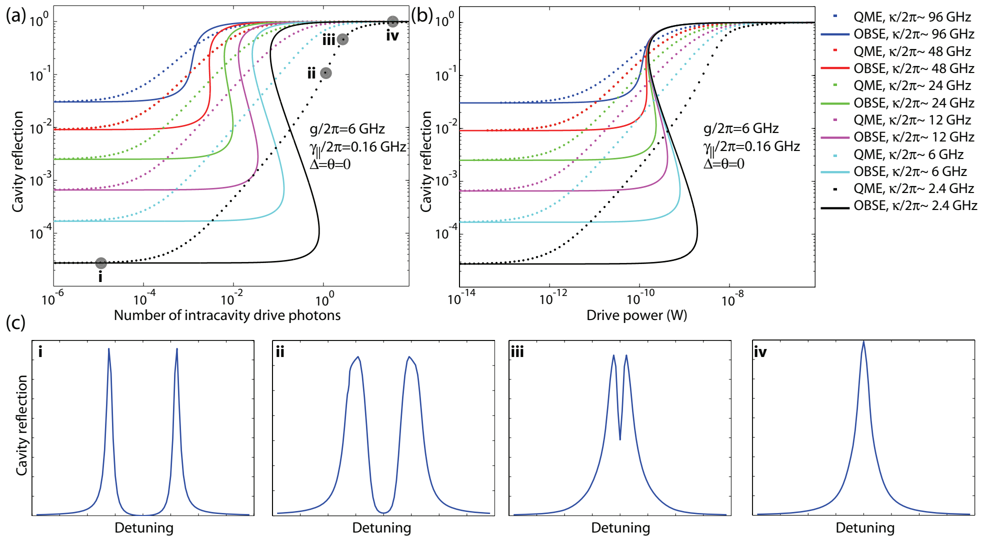


Figure 8.12: Steady state solutions to the semiclassical Maxwell-Bloch equations (solid lines) and quantum master equation (dots), showing cavity reflection as a function of (a) average number of intracavity drive photons (b) input drive power, for varying cavity decay rates. In these simulations, $\omega_a = \omega_c = \omega_l$, and $g/2\pi$=6 GHz. We assume $\gamma_p$=0, and $\gamma_{||}/2\pi$=0.16 GHz. The cavity reflection spectrum at selected drive strengths, indicated by the gray circles in (a) and labeled i-iv, are shown in (c).

temperature, where non-radiative dephasing of the QD broadens its linewidth, to values on the order of ∼5 meV (for a QD exciton line at ∼1 eV). Equation (8.21) predicts $m_0$ ∼0.4 for $g/2\pi$ ∼10 GHz, indicating that a single photon can still have an appreciable effect on a single QD. However, the significant non-radiative dephasing would also suggest that any switching devices will not function as efficiently as they do at low temperature.

We first plot $X_{ss}$ as a function of $Y$ (fig. 8.13(a)) for a system with $g/2\pi$=17 GHz and $\kappa/2\pi$=0.1 GHz. We now see that neither the semiclassical nor the quantum master equation solutions display bistability, and that the two solutions match much more closely than they did in the previous example. Despite the absence of bistability, the shape of the curve is very similar to the quantum master equation solution in the radiative-limited case, indicated the potential for switching between low reflection and high reflection values at relatively low powers.

The reflected signal from the cavity as a function of average number of intracavity drive photons and input drive power for a couple of different combinations of $\kappa$ and $g$ are plotted in fig. 8.14. These solutions indicate that low switching powers can still be achieved, but that the reflection contrast is significantly diminished as a result of the non-radiative dephasing. Relatively large cavity $Q$s ($> 10^6$) are then needed to achieve ∼20 dB of contrast. As mentioned above, switching in the

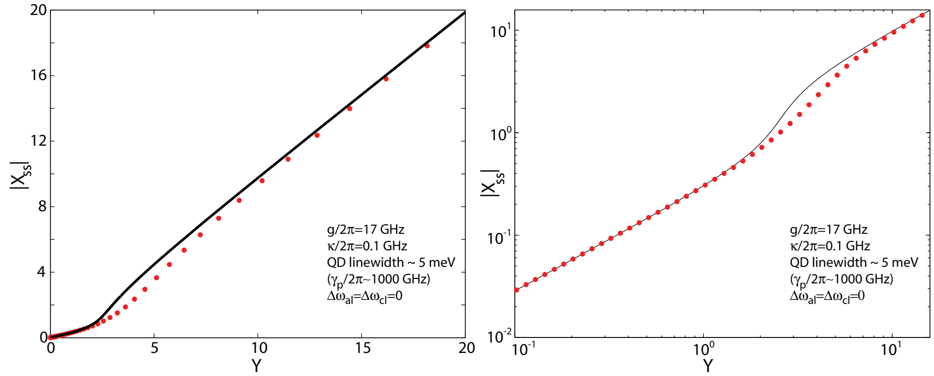


Figure 8.13: Steady state solutions to the semiclassical Maxwell-Bloch equations (solid line) and quantum master equation (dots), showing normalized intracavity field amplitude $|X_{ss}|$ as a function of normalized drive field $|Y|$, for a system with large non-radiative dephasing (linewidth $\sim 5$ meV).

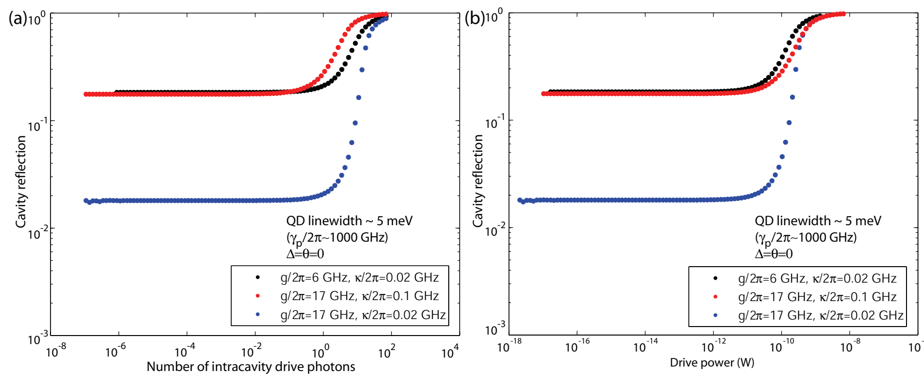


Figure 8.14: Steady state solutions to the quantum master equation, showing cavity reflection as a function of (a) average number of intracavity drive photons and (b) input drive power (right), for a system with large non-radiative dephasing (linewidth $\sim 5$ meV). In these simulations, $\omega_a = \omega_c = \omega_l$.

transmitted signal can be achieved by tuning the drive field to $\omega_l = \pm g$.

The simulations presented above are just a preliminary examination of switching possibilities in these fiber-coupled microcavity-QD systems. A more detailed bifurcation analysis of the semiclassical model and quantum trajectory analysis to study the time-dependent properties of the system must be conducted better understand the system and the various types of behavior that can be accessed for different parameter regimes. The recent analysis of Armen and Mabuchi [178] will be quite useful in this regard.